

## MODELING AND DESIGN OPTIMIZATION OF A RESONANT OPTOTHERMOACOUSTIC TRACE GAS SENSOR\*

NOEMI PETRA<sup>†</sup>, JOHN ZWECK<sup>‡</sup>, SUSAN E. MINKOFF<sup>‡</sup>, ANATOLIY A. KOSTEREV<sup>§</sup>,  
AND JAMES H. DOTY III<sup>§</sup>

**Abstract.** Trace gas sensors that are compact and portable are being deployed for use in a variety of applications including disease diagnosis via breath analysis, monitoring of atmospheric pollutants and greenhouse gas emissions, control of industrial processes, and for early warning of terrorist threats. One such sensor is based on optothermal detection and uses a modulated laser source and a quartz tuning fork resonator to detect trace gases. In this paper we introduce the first mathematical model of such a resonant optothermoacoustic sensor. The model is solved via the finite element method and couples heat transfer and thermoelastic deformation to determine the strength of the generated signal. Numerical simulations validate the experimental observation that the source location that produces the maximum signal is near the junction of the tines of the tuning fork. Determining an optimally designed sensor requires maximizing the signal as a function of the geometry of the quartz tuning fork (length and width of the tines, etc). To avoid difficulties from numerical differentiation we chose to solve the optimization problem using the derivative-free mesh adaptive direct search algorithm. An optimal tuning fork constrained to resonate at a frequency close to the 32.8 kHz resonance frequency of many commercially available tuning forks produces a signal that is three times larger than the one obtained with the current experimental design. Moreover, the optimal tuning fork found without imposing any constraint on the resonance frequency produces a signal that is 24 times greater than that obtained with the current sensor.

**Key words.** trace gas sensing, optothermal detection, linear thermoelasticity, design optimization, mathematical modeling

**AMS subject classifications.** 35J05, 65K10, 74F05, 74S05, 80A20, 80M10

**DOI.** 10.1137/100807181

**1. Introduction.** Trace gas sensors are the modern day equivalent of the proverbial canary in the coalmine. In addition to detecting and identifying harmful gases such as carbon monoxide and methane in industrial workplaces, networks of trace gas sensors are being used to monitor environmental pollutants [27] and greenhouse gases such as carbon dioxide [57]. In the future, the diagnosis of diseases will benefit from ongoing research to develop compact and portable breath analyzers that will replace or supplement blood testing and biopsies [34, 46]. Such sensors are especially important for diseases such as lung cancer [34] for which diagnosis protocols do not yet exist.

Since molecules absorb light at characteristic wavelengths, most spectroscopic trace gas sensors are based on measuring this absorption. Two of the more common

---

\*Received by the editors September 1, 2010; accepted for publication (in revised form) December 2, 2010; published electronically February 24, 2011. This research was funded by the U.S. National Science Foundation through the MIRTHER-ERC program (grant EEC-0540832). The hardware used in the computational studies was supported by the UMBC High Performance Computing Facility (HPCF), funded by the NSF through the MRI program (grant CNS-0821258) and the SCREMS program (grant DMS-0821311), with additional support from UMBC.

<sup>†</sup><http://www.siam.org/journals/siap/71-1/80718.html>

<sup>‡</sup>Institute for Computational Engineering and Sciences, The University of Texas at Austin, Austin, TX 78712 (noemi@ices.utexas.edu).

<sup>§</sup>Department of Mathematics and Statistics, University of Maryland Baltimore County, 1000 Hilltop Circle, Baltimore, MD 21250 (zweck@umbc.edu, sminkoff@umbc.edu).

<sup>§</sup>Department of Electrical and Computer Engineering, Rice University, 6100 Main Street, Houston, TX 77005 (akoster@rice.edu, jim.doty@rice.edu).

types of spectroscopy sensors are the sensors which measure the attenuation of light after transmission through a gas [27] and photoacoustic spectroscopy sensors which detect the weak acoustic pressure waves that are generated when optical radiation is periodically absorbed by the gas molecules [8, 9, 36]. It is also possible to design optothermal sensors which detect thermal diffusion waves generated by the periodic interaction of a laser with a gas [55]. As the books and survey articles by Mandelis demonstrate, mathematical models and engineering applications for diffusion waves have been extensively studied [30, 31, 32]. This paper deals with a new optothermal sensing method called Resonant OptoThermoAcoustic DEtection (ROTADE) [12, 23, 25, 43]. With ROTADE sensing the thermal diffusion wave excites a resonant acoustic vibration in a quartz tuning fork (QTF) detector.

In this paper, we present the first mathematical model of a ROTADE sensor. Although initial experimental tests have proven promising [12, 25], mathematical models are needed to extend the physical understanding of the ROTADE sensing method, to quantify how the strength of the ROTADE signal depends on the system parameters, and to numerically optimize the design of these sensors. Our model consists of three stages. First, we use the heat equation to model the periodic transfer of energy from the laser source into the interior of the QTF and the induced periodic change in temperature in the QTF. Then, we use thermoelasticity theory [10] to model the resonant vibration of the tuning fork that is induced by this periodic temperature change. Finally, we use the piezoelectric properties of quartz to compute the received electrical current generated by this vibration [44].

Since quartz tuning forks have long been used in clocks [33], most prior modeling work has focused on designing QTFs that resonate at  $2^{15}$  Hz ( $\approx 32$  kHz) [21, 52]. For example, a sensitivity analysis and parameter study performed by Lee [28] showed that the precise resonance frequency of a 32 kHz QTF depends strongly on the width and the length of the tines but only weakly on other geometric design parameters. QTFs have also been used for atomic-force and optical near-field microscopy [18, 22, 49]. In these applications, a sharp tip or an optical fiber attached to a tine of a QTF is kept at a fixed distance from a nanoscale surface being scanned by using the resonant vibration of the QTF to detect shear forces between the fiber and the surface. Karraï and Grober [22] found that it was sufficient to use a phenomenological forced harmonic oscillator model to mathematically optimize these QTF-based systems.

While other researchers have developed optothermal trace gas sensors, ROTADE sensors are the first devices that use QTFs to detect thermal diffusion waves. Vasilenko, Kovalev, and Rubtsova [55] designed a sensor to detect carbon dioxide via the optothermal heating of a pyroelectric plate mounted on the wall of a gas cell. The authors were able to increase the signal strength of the detector with the aid of a one-dimensional heat transfer model. The modeling of devices that rely on thermoelastic phenomena is also receiving increased attention. For example, Pelesko [40, 41] and Quinn and Pelasco [45] developed a nonlinear stability theory for thermoelastic contact and Ahmad, Upadhyay, and Venkatesan [4] described a thermoelastic finite element model to control structural deformations of smart matter structures.

The work that is most closely related to that presented here is on the modeling of quartz-enhanced photoacoustic spectroscopy (QEPAS) sensors by Wojcik et al. [56], Petra et al. [44], and Firebaugh, Roignant, and Terray [13, 14]. Wojcik et al. [56] computed the acoustic pressure wave in a QEPAS sensor using both a Green's function's approach in free space and an eigenfunction expansion in a cylindrical shell. They also outlined an approach for calculating the piezoelectric current induced in the QTF by the acoustic wave. However, Wojcik et al. did not use their model to

quantify how the signal depends on the system parameters. Firebaugh, Roignant, and Terray [13, 14] developed a fully numerical model of a QEPAS sensor with a microresonator which they used to determine the dependence of the signal on the length of the microresonator. QEPAS and ROTADE sensors are both being developed by Kosterev [23], Kosterev et al. [24], and Kosterev and Doty [25], and they both use a QTF to detect trace gases. However, with QEPAS sensing, the QTF responds to acoustic pressure waves rather than to thermal diffusion waves. As we will explain in section 2, QEPAS and ROTADE are complementary techniques. Although the ROTADE signal is usually much weaker than the QEPAS signal, in some circumstances, such as at low gas pressure (i.e.,  $\lesssim 50$  Torr (6.67 kPa)), the sensor can be configured so that the ROTADE signal dominates. In this situation, ROTADE is also more highly selective than QEPAS; i.e., it can better differentiate between trace gases. Both sensors are compact, portable, and as sensitive as traditional detectors.

Petra et al. [44] developed and validated a model of a QEPAS sensor and used it to show that the signal strength is largest when the laser source is positioned near the tip of the QTF. For that model, we made several simplifying assumptions to reduce the partial differential equations in the model to ordinary differential equations which we solved analytically. Since these assumptions are not valid for ROTADE sensors, in this paper we obtain a numerical solution of a coupled model based on three-dimensional heat transfer and thermoelasticity theory. We use the ROTADE model developed in this paper to study how the amplitude and phase of the ROTADE signal depend on the position of the laser source. Our results show that the signal is largest when the laser is positioned near the base of the QTF. We validate the model by obtaining good agreement with experimental results for 0.5% acetylene in nitrogen. However, a comparison with experiments using pure carbon dioxide suggests that, when the gas to be detected has a high concentration, the classical heat equation may need to be replaced by an equation that more accurately models the molecular dynamics of the gas.

Finally, we use mathematical optimization to determine the geometry of the QTF that maximizes the signal response of a ROTADE sensor. We perform the optimization using the derivative-free mesh adaptive direct search (MADS) algorithm for solving nonlinear optimization problems with general nonlinear constraints [3, 7]. We used a derivative-free optimization method since the objective function is computed by numerically solving partial differential equations which can lead to difficulties in accurately differentiating the objective function with respect to the system parameters. The optimization problems we solve include a frequency-constrained problem, in which we fix the QTF resonance frequency close to 32.8 kHz, and a frequency-unconstrained problem, in which we search for the optimal geometry of the QTF without constraining the resonance frequency. The motivation for solving a frequency-constrained problem is that the great majority of commercially available QTFs oscillate at 32.8 kHz frequency; hence our model could be used to select the best QTF available on the market. The optimization results show that, while the frequency-constrained problem gives a signal that is three times larger than the one obtained with the standard 32.8 kHz QTF we used in the experiments, when the frequency can vary the optimal solution is 24 times greater.

The remaining sections of this paper are organized as follows. In section 2 we describe the physics of ROTADE sensors, and in section 3 we present the mathematical model we developed for these sensors. The formulation of the QTF design optimization problem is given in section 4. In sections 5 and 6 we give a description of the finite element solution of the coupled model as well as details on how the optimization

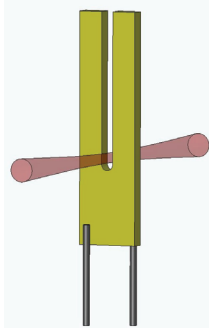


FIG. 1. Schematic diagram of the experimental setup for a ROTADE sensor showing the tuning fork (the “U”-shaped bar with two tines), two attached wires, and the laser source focused between the tines of the tuning fork.

problems are solved and our numerical results.

**2. The physics of ROTADE sensors.** Molecular gases, such as carbon dioxide and acetylene, can be characterized by their absorption spectra. With many gas sensing methods, including the ROTADE method, a particular gas is detected by making measurements at a single wavelength. This wavelength can be chosen by comparing the absorption spectrum of the gas to be detected with the spectra of other common trace gases [48]. Initial results by Doty, Kosterev, and Tittel [12] suggest that ROTADE sensors are optothermal detectors; i.e., they detect thermal diffusion waves that are generated by the periodic interaction of optical radiation with a trace gas. Specifically, the underlying physical mechanism involves the following processes: A laser generates optical radiation at a specific absorption wavelength of the gas that is to be detected. The laser beam is directed between the tines of a QTF (see Figure 1). The optical energy that is absorbed by the trace gas is transformed into vibrational energy of the gas molecules. This vibrational energy is transported to the surface of the QTF via diffusion of the excited molecules. Upon collision with the surface, the excited molecules transfer vibrational energy to the QTF in the form of heat. The probability that a gas molecule will transfer its energy and the fraction of energy that is transferred depends on the distribution of energy among the vibrational, rotational, and translational degrees of freedom of the gas. The thermal energy transferred to the surface then diffuses into the interior of the QTF where it induces a mechanical stress and displacement of the tines of the QTF. Because the wavelength (or, alternatively, the power) of the laser is modulated at an appropriate frequency, a mechanical resonance is excited in the QTF. Since quartz is a piezoelectric material, this mechanical vibration is converted into a charge separation on electrodes that are attached to the surface of the QTF. Finally, an electric circuit is used to convert the charge separation to an electric current that is measured. In summary, a ROTADE sensor system utilizes a combination of the thermoelastic effect, in which heat generates mechanical stress, and the piezoelectric effect, in which this stress generates an electric displacement. The combination of these two effects is called the indirect pyroelectric effect [39]. One of the goals of this paper is to use modeling to validate this physical understanding of ROTADE sensors.

ROTADE sensors are closely related to QEPAS sensors which rely on the photoacoustic effect, that is, on the conversion of optical radiation to an acoustic pressure wave [8, 9, 47]. This conversion relies on vibrational-to-translational (V-T) energy

transfer processes at the molecular level. With QEPAS, the QTF is driven by an external force due to the pressure difference between the inner and outer surfaces of the QTF [44].

QEPAS and ROTADE are complementary techniques. In fact the same QTF can be used to detect both the QEPAS and ROTADE signals, and both physical processes occur simultaneously, although one is usually dominant. The relative strength of these two signals is primarily determined by the ambient pressure and, as we show in this paper, by the position of the laser beam relative to the base of the QTF. At atmospheric pressure we expect that QEPAS will be dominant since, as the distance from the axis of the laser beam increases, the diffusion wave decays much more rapidly than does the acoustic wave. However, as the ambient pressure and density are lowered, the frequency of molecular collisions decreases, lowering the V-T relaxation rates and the efficiency of the conversion of molecular vibrational energy to acoustic energy. Therefore, ROTADE is expected to be more sensitive than QEPAS when the ambient pressure is low enough ( $\lesssim 50$  Torr (6.67 kPa)). At low ambient pressure the lines in the absorption spectrum become more distinct, thus providing ROTADE sensors with more wavelength selectivity than other sensors. As the ambient pressure increases, the absorption lines broaden, and closely spaced lines can overlap.

With both QEPAS and ROTADE systems the strength of the received signal is proportional to the concentration of the trace gas, provided that the signal-to-noise ratio is large enough [20]. Designing sensor systems that can measure extremely low gas concentrations is a technological challenge. ROTADE sensor systems attempt to address this challenge through a combination of new sensor technologies and design optimization. First, molecules have much stronger absorption lines in the infrared region than in the visible region of the electromagnetic spectrum where most traditional lasers operate. ROTADE sensor systems will incorporate a recently developed breed of laser—the quantum cascade laser [20]—that enables much greater access to the infrared region than was previously available. Access to the infrared is also facilitated by the use of a QTF detector, since the QTF responds to the frequency of wavelength modulation about an absorption line rather than to the wavelength of the absorption line itself. Second, ROTADE sensors utilize the very strong mechanical resonances of QTFs. Consequently, the quality factor—which measures the strength of the resonance [15]—is on the order of  $Q \simeq 15,000$  at an ambient pressure of 450 Torr (60 kPa) and in excess of 30,000 at pressures less than 50 Torr (6.67 kPa) [44]. In addition, QEPAS and ROTADE sensors are immune to environmental thermal and acoustic noise since they operate by exciting the fundamental symmetric mode of vibration in which the tines move in opposite directions in the plane of the QTF [44]. With this mode of vibration, noise from sources located far from the QTF is canceled in the received electrical signal due to destructive interference. Another advantage of QEPAS and ROTADE sensors is that the volume of a standard QTF (resonating at 32 kHz) is only  $3 \text{ mm}^3$ , whereas the volume of traditional photoacoustic detectors [37] is about 1000 times larger.

**3. Mathematical model.** Our computational model of a ROTADE sensor consists of three stages. First, we compute the change in temperature in the three-dimensional tuning fork due to the interaction between the laser and gas sample. Then we study the induced deformation of the tuning fork, and finally we compute the generated electrical signal. We now explain the three stages of the model in more detail.

**3.1. Model of the optically generated thermal wave.** We use the classical heat equation to model both the diffusion of excited gas molecules to the surface of the QTF and the resulting diffusion of heat into the interior of the QTF. In particular, we ignore the dynamics of energy exchange processes between the different degrees of freedom of the diffusing gas molecules. We also assume that all the energy of each gas molecule that is in excess of the ambient thermal energy is transferred to the surface in every collision. That is, we assume that the heat is transferred to the surface of the QTF as if the gas were in thermal equilibrium and therefore that the temperature varies continuously across the boundary surfaces of the QTF. Although the absolute temperature is not accurately represented in this simplified model, we still expect that the model will capture the trends observed in experimental data.

The heat equation is given by

$$(3.1) \quad \frac{\partial T}{\partial t} - \nabla \cdot (\kappa \nabla T) = S_T,$$

where  $T = T(\mathbf{x}, t)$  is the temperature,  $\mathbf{x}$  denotes position in  $\mathbb{R}^3$ , and  $t$  is time. The thermal diffusivity tensor,  $\kappa$ , is given by  $\kappa = K/\rho c_p$ , where  $\rho$  is the density,  $c_p$  is the specific heat capacity, and  $K$  is the thermal conductivity tensor of the medium. In quartz, which is a trigonal crystal, the tensor  $K$  is a  $3 \times 3$  diagonal matrix with diagonal entries  $K_1, K_1$ , and  $K_3$  [16, 39]. The thermal source,  $S_T$ , is modeled by

$$(3.2) \quad S_T(\mathbf{x}, t) = \frac{\alpha_{\text{eff}} W_L}{\rho c_p \pi w^2(y)} \exp\left(-\frac{2[(x - x_s)^2 + (z - z_s)^2]}{w^2(y)}\right) \exp(i\omega t).$$

The thermal wave is then the real part of the solution of (3.1). Here  $\alpha_{\text{eff}}$  is the effective absorption coefficient of the gas, and  $W_L$  is the total laser power [44]. The function  $w(y)$  models the width of the Gaussian beam via the formula

$$(3.3) \quad w(y) = w_0 \sqrt{1 + \left(\frac{y}{y_R}\right)^2},$$

where  $w_0$  is the width of the Gaussian beam at the origin,  $y_R = \pi w_0^2/\lambda$  is the Rayleigh length, and  $\lambda$  is the wavelength of the radiation [50]. The coordinate system we use for the QTF is shown in Figure 2. The laser beam points in the  $y$  direction and passes through the point  $(x_s, z_s)$ . For the remainder of this paper we will use the notation  $f$  or  $f(x)$  to denote the spatial part of  $f(x, t)$  with the understanding that  $f(x, t) = f(x) \exp(i\omega t)$ . Whether or not  $f$  depends on time will be understood from the context. Therefore in order to find the time harmonic solution of (3.1)–(3.2) we solve the associated Helmholtz equation

$$(3.4) \quad -\nabla \cdot (\kappa \nabla T) + i\omega T = S_T.$$

**3.2. Model for the vibration of the tuning fork.** The thermal wave generated by the absorption of optical energy induces a thermal stress in the quartz which causes the tuning fork to vibrate. In this section, we present the second stage of the model, namely that which describes the deformation of the tuning fork. The thermo-elastic deformation of a QTF is governed by the stress-strain-temperature relation, the strain-displacement relation, and the equation of motion [10], given, respectively, by

$$(3.5) \quad \begin{cases} S &= C[E] - C[\alpha T], \\ E &= \frac{1}{2}(\nabla \mathbf{u} + \nabla \mathbf{u}^T), \\ \nabla \cdot S &= \rho \ddot{\mathbf{u}}. \end{cases}$$

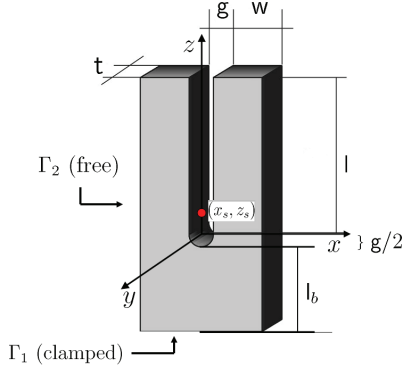


FIG. 2. The coordinate system and geometric parameters of a QTF. The dimensions of the tuning fork are  $l$  (length),  $g$  (gap),  $t$  (thickness),  $w$  (width), and  $l_b$  (length of the base). The origin of the QTF coordinate system is chosen so that the front and back faces of the QTF are at  $y = \pm t/2$  and the axis of the semicylindrical surface near the junction of the two tines passes through the origin; i.e., the center of the semicircle in the  $xz$ -plane is at  $(0, 0)$ . The laser beam axis is parallel to the  $y$  and passes through the point  $(x_s, z_s)$  in the  $xz$ -plane. The fixed and free boundaries of the tuning fork are denoted by  $\Gamma_1$  and  $\Gamma_2$ , respectively.

Here the column vector  $\mathbf{u} = (u, v, w)^T$  is the displacement vector field, and  $T$  is the temperature. The stress and strain tensors are denoted by  $S$  and  $E$ , respectively, and  $\rho$  is the density of the medium. Both  $S$  and  $E$  are second-order tensors which are represented by  $3 \times 3$  matrices in (3.5). The fourth-order tensor  $C$  is the elasticity tensor which is a linear transformation from the space of all symmetric second-order tensors to itself. The thermal expansion coefficient tensor,  $\alpha$ , is a second-order symmetric tensor that quantifies the change in volume of the material if it is heated in the absence of stress. Since quartz is a trigonal crystal, the matrix representation of  $\alpha$  is a  $3 \times 3$  diagonal matrix with entries  $\alpha_1, \alpha_1$ , and  $\alpha_3$  [16, 39].

Because the displacement is expected to be small, we may assume that  $C[E] = C[\nabla \mathbf{u}]$  [10]. To phenomenologically incorporate damping into the model we add a resistive force proportional to the velocity. Here the damping constant is defined by  $b = \rho \omega_0 / Q$ , where  $\omega_0$  is the resonance frequency without damping, and  $Q$  is the measured quality factor of the tuning fork [15]. Then the above equations combine to yield the displacement-temperature equation

$$(3.6) \quad \rho \frac{\partial^2 \mathbf{u}}{\partial t^2} + b \frac{\partial \mathbf{u}}{\partial t} - \nabla \cdot C[\nabla \mathbf{u}] = -\nabla \cdot C[\alpha T].$$

We suppose that the tuning fork is fixed at the bottom (i.e., on the surface  $\Gamma_1$  in Figure 2) and that the traction is zero [10] on the remaining surfaces (i.e., on  $\Gamma_2$ ). Then the Helmholtz boundary value problem that models the temperature-driven elastic deformation of the QTF is given by

$$(3.7) \quad \begin{cases} \nabla \cdot C[\nabla \mathbf{u}] + (\rho \omega^2 - ib\omega) \mathbf{u} &= \nabla \cdot C[\alpha T] & \text{in } \Omega_{\text{TF}}, \\ \mathbf{u} &= 0 & \text{on } \Gamma_1, \\ C[\nabla \mathbf{u}] \mathbf{n} &= C[\alpha T] \mathbf{n} & \text{on } \Gamma_2, \end{cases}$$

where  $\Omega_{\text{TF}}$  is the three-dimensional domain of the tuning fork, and  $\mathbf{n}$  is the outward unit normal vector field to  $\Gamma_2$ .

**3.2.1. Eigenfrequency analysis.** The electrodes attached to the surfaces of the tuning fork are configured in such a way that only the symmetric mode of vibration (in which the tines move out symmetrically with respect to the plane of symmetry of the tuning fork) induces an electrical signal. To numerically determine this eigenfrequency we solve the eigenvalue problem

$$(3.8) \quad \begin{cases} \nabla \cdot C[\nabla \mathbf{u}] + \rho\omega_0^2 \mathbf{u} = 0 & \text{in } \Omega_{\text{TF}}, \\ \mathbf{u} = 0 & \text{on } \Gamma_1, \\ C[\nabla \mathbf{u}] \mathbf{n} = 0 & \text{on } \Gamma_2. \end{cases}$$

We use this model to compute the eigenfunctions and select the one that corresponds to the symmetric motion of the tines. We use the eigenfrequency,  $\omega_0$ , corresponding to this eigenfunction as an input parameter to both the heat and deformation models described in sections 3.1 and 3.2, respectively.

**3.3. Model of the piezoelectric response of the tuning fork.** In this section, we present the third stage of the model, namely that which relates the amplitude of oscillation of each tine of the tuning fork to the induced piezoelectric signal. We verified that, at the resonance frequency,  $\omega_0$ , the motion of the QTF is symmetric, even when the laser is positioned off of the plane of symmetry. As we explained in [44], the charge,  $q(t)$ , generated on one tine of the tuning fork is related to the  $x$ -component of the displacement,  $u_L$ , of a point,  $p$ , on the tip of that tine by  $q = \nu u_L$ , where  $\nu$  is the effective piezoelectric coupling constant. Because of the symmetry of the motion of the tines, the amplitude of the piezoelectric current generated by the QTF is then

$$(3.9) \quad I = 2\nu v_L = 2\nu\omega u_L,$$

where  $v_L$  is the  $x$ -component of the velocity of the tip. Similarly, the phase of the current can be obtained from that of  $u_L$ .

**4. Formulation of the optimization problem.** In this section, we formulate both frequency-constrained and frequency-unconstrained optimal design problems for the QTF. Our goal is to find the geometric parameters (length ( $l$ ), width ( $w$ ), gap ( $g$ ), length of the base ( $l_b$ ), and thickness ( $t$ )) that maximize the velocity,  $v_L$ , of the tines of the QTF given by

$$(4.1) \quad v_L = \omega u_L,$$

where  $u_L$  is the  $x$ -component of displacement of the tuning fork tip. By (3.9), the signal is proportional to the effective piezoelectric coupling constant,  $\nu$ . The noise is also proportional to  $\nu$  since it is dominated by Johnson noise associated with mechanical dissipation in the QTF [18, 26]. Since the quantity of interest is the signal-to-noise ratio [24, 27], it is therefore reasonable to maximize the velocity of the tip of the tines rather than the piezoelectric current itself.

Since most commercially available QTFs operate at or close to 32.8 kHz, for the frequency-constrained problem we require the resonance frequency,  $f$ , of the tuning fork to lie between  $f^l = 30$  kHz and  $f^u = 34$  kHz. The objective function,  $J : \mathbb{R}^5 \rightarrow \mathbb{R}$ , is defined by the nonlinear function  $J(\mathbf{p}) = -v_L(\mathbf{p}, f(\mathbf{p}))$ , where the parameter vector is  $\mathbf{p} = (l, w, g, l_b, t)$ . For the frequency-unconstrained problem the search space,  $X_u$ , is the subset of  $\mathbb{R}^5$  given by

$$X_u = [l^l, l^u] \times [w^l, w^u] \times [g^l, g^u] \times [l_b^l, l_b^u] \times [t^l, t^u],$$

and for the frequency-constrained problem the search space is

$$X_c = \{\mathbf{p} \in X_u \mid f^l < f(\mathbf{p}) < f^u\}.$$

Then the minimization problems are given by

$$(4.2) \quad \begin{aligned} &\text{minimize} && J(\mathbf{p}) \\ &\text{subject to} && \mathbf{p} \in X, \end{aligned}$$

where  $X = X_u$  or  $X = X_c$  as appropriate.

**5. Numerical solution method.** In this section, we present the numerical techniques used to solve the equations which model the ROTADE sensor. The partial differential equations involved in the models were solved using the COMSOL Multiphysics finite element solver package [11]. To accurately compute the rapid decay of the temperature and the thermal stress we used Lagrange quadratic finite elements on tetrahedral meshes. Since high resolution is required only near the source location, we used adaptive mesh refinement to reduce the number of unknowns. Because the discretization of the thermal problem leads to a linear system that involves non-Hermitian matrices, we solved the system using the GMRES (generalized minimal residual) iterative solver [17, 54]. The eigenvalue and deformation problems were solved using the SPOOLES (SParse Object Oriented Linear Equations Solver) direct solver [5]. The parameter studies were performed using the scripting capabilities of COMSOL in conjunction with MATLAB [42].

For the numerical optimization simulations, we used the NOMAD optimization software [2]. NOMAD is a derivative-free optimization package built primarily on the MADS algorithm and tuned to obtain the optimal solution with a small number of objective function evaluations. The objective function evaluations were performed using COMSOL to solve the ROTADE partial differential equation model. The coupling of our COMSOL code and NOMAD was accomplished by using NOMADm, the MATLAB implementation of NOMAD.

**5.1. Simulation method for the heat problem.** To compute the heat distribution using the finite element method we must solve the Helmholtz equation (3.4) in a finite computational domain,  $\Omega$ , which we decompose as  $\Omega = \Omega_{\text{TF}} \cup \Omega_{\text{gas}}$ , where  $\Omega_{\text{TF}}$  and  $\Omega_{\text{gas}}$  are subdomains containing the tuning fork and the gas surrounding it, respectively (see Figure 3). We recall that the laser beam axis is parallel to the  $y$ -axis and passes between the tines of the tuning fork. To impose appropriate boundary conditions we decompose the boundary of  $\Omega$  as  $\partial\Omega = \Gamma_{\text{fb}} \cup \Gamma_{\text{side}}$ , where  $\Gamma_{\text{fb}}$  consists of the front and back surfaces of  $\partial\Omega$ , i.e., those that are parallel to the  $xz$ -plane, and  $\Gamma_{\text{side}}$  consists of the remaining boundary surfaces (see Figure 3). Because the solution decays very rapidly in the  $xz$ -plane as the radial distance from the axis of the laser beam increases, on  $\Gamma_{\text{side}}$  we impose zero boundary conditions. However, since the laser beam crosses  $\Gamma_{\text{fb}}$ , we set the boundary condition for  $T$  on  $\Gamma_{\text{fb}}$  to be  $T = T_{\text{bdy}}$ , where  $T_{\text{bdy}}$  solves a two-dimensional heat problem with a heat source given by (3.2) evaluated on  $\Gamma_{\text{fb}}$  and zero Dirichlet boundary conditions on  $\partial\Gamma_{\text{fb}}$ . Therefore, if the domain  $\Omega$  is large enough, the resulting solution will be a good approximation to the true solution in  $\mathbb{R}^3$  because of the rapid decay of the temperature.

**5.2. Numerical optimization method.** We use the MADS algorithm to solve the optimization problems given by problem (4.2). The MADS algorithm is an extension of pattern search methods [1, 6, 53, 29] for nonlinearly constrained optimization

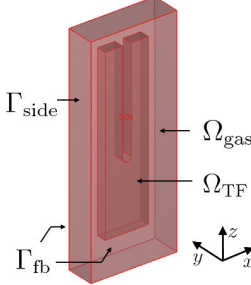


FIG. 3. Computational domain for the heat transfer problem.

problems. The discussion on the MADS algorithm that follows comes from the papers by Audet and Dennis [6, 7]. The algorithm starts at iteration  $k = 0$  with an initial point,  $\mathbf{p}_0$ , and an initial mesh size,  $\Delta_0$ . Each iteration  $k > 1$  consists of a search step and a poll step. The search step generates a finite number of trial points using the Latin hypercube sampling method [51]. The trial points are generated so as to lie on the mesh,  $M_k$ , defined by

$$(5.1) \quad M_k = \bigcup_{x \in S_k} \{x + \Delta_k Dz : z \in \mathbb{N}^{n_D}\}.$$

Here  $S_k$  denotes the set of points where the objective function,  $J$ , has already been evaluated by the start of iteration  $k$ , and  $\Delta_k$  is the current mesh size. Finally,  $D$  is an  $n \times n_D$  matrix ( $n_D \geq 2n$ ) whose rows positively span  $\mathbb{R}^n$ . Any trial points that do not lie in the search space  $X_u$  are discarded. If there exists a trial point with a lower objective function value than the current incumbent value (i.e., the best objective value found so far), then the algorithm sets the incumbent to this lower value, coarsens the mesh by setting  $\Delta_{k+1} = 2\Delta_k$ , and proceeds to iteration  $k + 1$ . If no such trial point exists, then the poll step is invoked before terminating the iteration.

The poll step reduces the mesh size by half and generates trial points on a related mesh called a “poll frame” defined by

$$(5.2) \quad P_k = \{x_k + \Delta_k D e_i : i = 1, \dots, n_D\} \subset M_k,$$

where  $x_k$  is the current incumbent point, and  $e_i$  is the  $i$ th column of the identity matrix. The difference between the poll frame  $P_k$  and the search mesh  $M_k$  is that  $P_k$  is defined in terms of the unscaled directions of  $D$ . Among the feasible trial points, the poll step chooses the one with the lowest objective value as the incumbent point, sets the mesh size to  $\Delta_{k+1} = 0.5\Delta_k$ , and starts iteration  $k + 1$ . If no such trial point exists, the poll step is repeated until the objective function is reduced or the mesh size falls below a threshold value. The iterations stop when a stopping criterion is satisfied, and the optimal solution is declared to be the current incumbent point.

**5.3. Parameters involved in the model.** In this section, we provide the values of the parameters used in the laboratory experiments. The coordinate system and geometric parameters of a QTF are shown in Figure 2. These parameters are length ( $l$ ), gap ( $g$ ), thickness ( $t$ ), width ( $w$ ), and length of the base ( $l_b$ ). We used two gases in the laboratory experiments: 0.5% acetylene in nitrogen ( $\text{C}_2\text{H}_2:\text{N}_2$ ) and

TABLE 1

*Measured physical parameters from experiments:  $\omega$  (angular frequency),  $l$  (length),  $g$  (gap),  $t$  (thickness),  $w$  (width),  $\lambda$  (wavelength),  $W_L$  (laser power),  $\nu$  (effective piezoelectric coupling constant), and  $\alpha_{\text{eff}}$  (effective absorption coefficient of  $\text{CO}_2$ ).*

Parameter	Value	SI unit	Parameter	Value	SI unit
$\omega$	$2\pi \times 32785.47$	1/s	$\lambda$	$1.57 \times 10^{-6}$	m
$l$	$3.75 \times 10^{-3}$	m	$W_L$	$30 \times 10^{-3}$	W
$g$	$0.3 \times 10^{-3}$	m	$\nu$	$7 \times 10^{-6}$	C/m
$t$	$0.34 \times 10^{-3}$	m	$\alpha_{\text{eff}}$	0.04986	1/m
$w$	$0.6 \times 10^{-3}$	m			

TABLE 2

*Properties of quartz:  $\rho$  (density),  $c_p$  (specific heat capacity),  $K$  (thermal conductivity),  $\alpha$  (thermal expansion coefficient), and  $C$  (elastic moduli). The values of  $C$  were obtained from Gautschi [16].*

Parameter	Value	SI unit	Parameter	Value	SI unit
$\rho$	2650	kg/m <sup>3</sup>	$C_{11}$	$86.80 \times 10^9$	N/m <sup>2</sup>
$c_p$	733	J/(kgK)	$C_{12}$	$7.04 \times 10^9$	N/m <sup>2</sup>
$K_1$	6.5	J/(m s K)	$C_{13}$	$11.91 \times 10^9$	N/m <sup>2</sup>
$K_2$	6.5	J/(m s K)	$C_{14}$	$-18.04 \times 10^9$	N/m <sup>2</sup>
$K_3$	11.3	J/(m s K)	$C_{33}$	$105.75 \times 10^9$	N/m <sup>2</sup>
$\alpha_1$	$13.7 \times 10^{-6}$	1/K	$C_{44}$	$58.20 \times 10^9$	N/m <sup>2</sup>
$\alpha_2$	$13.7 \times 10^{-6}$	1/K	$C_{66}$	$39.88 \times 10^9$	N/m <sup>2</sup>
$\alpha_3$	$7.4 \times 10^{-6}$	1/K			

pure carbon dioxide ( $\text{CO}_2$ ). The experiments were run at the ambient pressure of 20 Torr (2.67 kPa). We list the experimental parameters in Tables 1, 2, and 3. For the numerical simulations we used the parameters for carbon dioxide and nitrogen ( $\text{N}_2$ ) and the  $Q$ -factor of the tuning fork at ambient pressures of 5, 10, and 20 Torr. The quality factor,  $Q$ , of an oscillatory system is given by  $Q = \omega_0/\gamma$ , where  $\omega_0$  is the angular frequency of the undamped oscillations and  $\gamma$  is the reciprocal of the time required for the energy to decrease to  $1/e$  of its initial value [15]. The  $Q$ -factor is approximately proportional to  $1/\sqrt{P}$  when the ambient pressure,  $P$ , is larger than about 10 Torr [19, 26]. From the ideal gas law, the density  $\rho$  is proportional to  $P$ . However, the thermal conductivity  $K$  is insensitive to variations in  $P$ .

**6. Results.** In this section, we describe the numerical simulations we performed to investigate the dependence of the piezoelectric signal on the position of the laser beam. These simulations were performed for carbon dioxide at an ambient pressure of 20 Torr. Then, we compare results from numerical simulations with those from laboratory experiments for the two gases: 0.5% acetylene in nitrogen and pure carbon dioxide.

**6.1. Numerical simulation results.** We first present the results of modeling the temperature distribution when the laser source is centered at  $(x_s, z_s) = (0, 0)$  (see Figure 2). On the left in Figure 4, we show the amplitude of the thermal wave on the

TABLE 3

Properties of (a)  $N_2$ , (b)  $CO_2$ , and (c) the  $Q$ -factor at ambient pressures of 5, 10, and 20 Torr:  $\rho$  (density),  $c_p$  (specific heat capacity),  $K$  (thermal conductivity), and  $\kappa$  (thermal diffusivity). The properties of  $N_2$  and  $CO_2$  were obtained with the aid of the NIST Chemistry WebBook [38].

Parameter	5 Torr	10 Torr	20 Torr	SI unit
(a) Properties of $N_2$				
$\rho$	0.007662	0.015168	0.030336	$kg/m^3$
$c_p$	1039.7	1039.7	1039.7	$J/kg K$
$K$	0.025367	0.025570	0.025570	$W/m K$
$\kappa$	0.003200	0.001600	0.0008107	$m^2/s$
(b) Properties of $CO_2$				
$\rho$	0.011915	0.023831	0.047664	$kg/m^3$
$c_p$	841.80	841.92	842.02	$J/kg K$
$K$	0.016437	0.016438	0.016438	$W/m K$
$\kappa$	0.001600	0.000819	0.000409	$m^2/s$
(c) The $Q$ -factor				
$Q$	79794	56423	39897	—

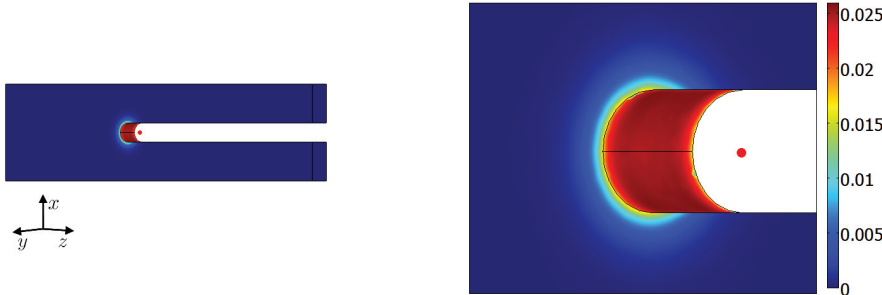


FIG. 4. Left: The numerical solution of the amplitude of the thermal wave on the surface of the QTF. Right: Zoomed in plot where the temperature is largest. For this simulation, the laser source was centered at  $(x_s, z_s) = (0, 0)$ . (The red dot shows the intersection of the laser beam axis with the  $xz$ -plane.)

surface of the QTF, and on the right we zoom in on the region where the temperature is largest. In Figure 5, we also show a one-dimensional slice of the temperature along the  $x$ -axis which confirms that the temperature decreases very rapidly once it reaches the QTF. This behavior is expected since the thermal diffusivity of carbon dioxide is higher than that of quartz by a factor of 100.

In Figure 6, we plot the normalized amplitude of the piezoelectric current as a function of frequency. The results show that the computed resonance frequency is about 33.8 kHz. In our simulations, for each position of the laser source, we first numerically computed the resonance frequency,  $\omega_0$ , of the tuning fork by solving the eigenvalue problem (3.8). Then, we used this value of  $\omega_0$  in the computation of the temperature,  $T$ , in (3.4) and the displacement,  $\mathbf{u}$ , in (3.7). For these simulations, it

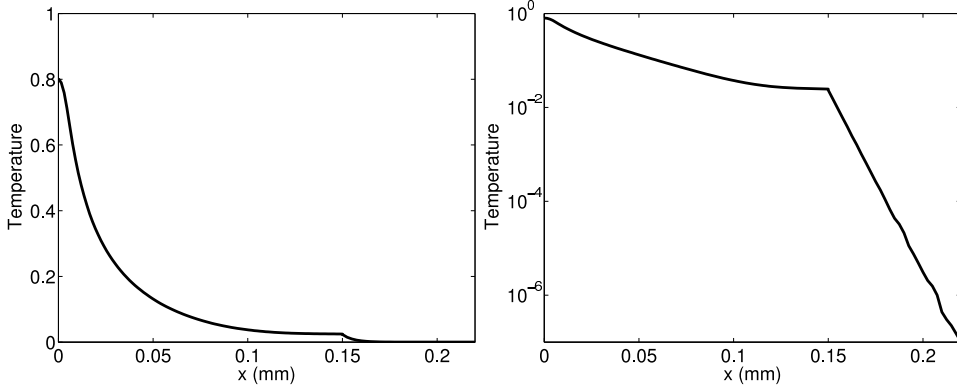


FIG. 5. One-dimensional slice of the temperature distribution computed in the exterior ( $0 < x < 0.15$  mm) and interior ( $x > 0.15$  mm) of the QTF. The slice is taken at  $(y, z) = (0, 0)$  and along the  $x$ -axis. For this simulation, the laser source was centered at  $(x_s, z_s) = (0, 0)$ , and the thermal source,  $S_T$ , was normalized to have value 1 at  $(0, 0, 0)$ . The right figure is a semilog plot of the temperature shown in the left figure.

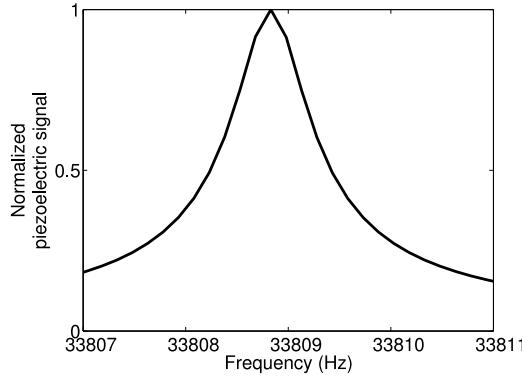


FIG. 6. The magnitude of the piezoelectric current as a function of frequency.

was important to use the same finite element mesh for the displacement computations as for the eigenanalysis.

Next we study how the piezoelectric signal strength depends on the laser source position  $(x_s, z_s)$ . We compute the piezoelectric current for the laser source positions shown with the three vertical lines in Figure 7. The origin of the coordinate system in Figure 7 is given by the solid circle. The circles, diamonds, and squares are located at 0.15, 0.03, and 0.013 mm, respectively, from the right vertical inner surface of the tuning fork. In Figure 8(left), we plot the normalized simulation results for the piezoelectric signal as a function of the  $z$ -coordinate of the laser position. The normalization was chosen so that at  $(x_s, z_s) = (0, 0)$  the piezoelectric signal is 1. For all three plots in Figure 8(left), as the laser source position,  $z$ , decreases from 0.8 mm to about 0 mm, the signal increases slightly, whereas as  $z$  decreases from 0 mm to  $-0.137$  mm (see Figure 7) the signal increases dramatically. We provide a physical explanation of these trends by considering the static case in which the temperature is independent of time. Since the temperature decays rapidly, the heat applied to the QTF is spatially localized about the point,  $p = p(x, z)$ , on the inner surface of the

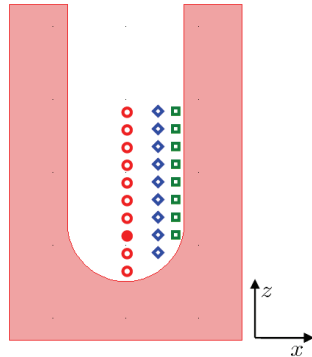


FIG. 7. Schematic of laser source positions for the simulation results shown in Figure 8. The location of the origin of the coordinate system is shown with the solid circle in the leftmost line of source positions.

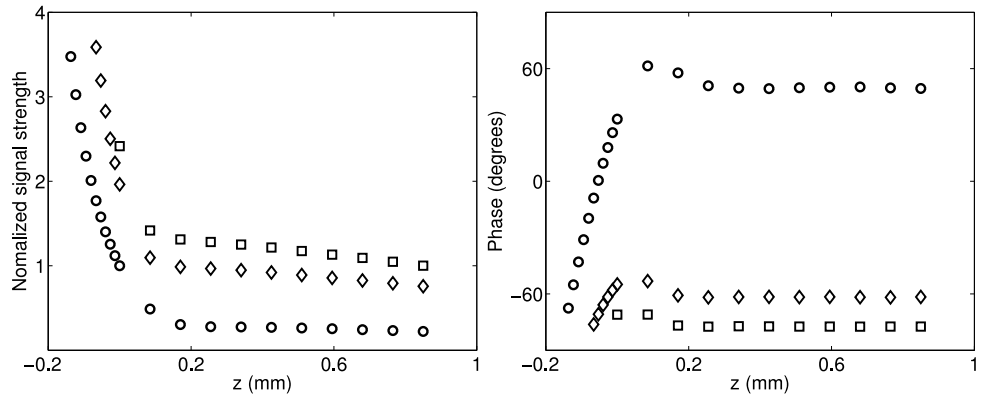


FIG. 8. Amplitude (left) and phase (right) of the piezoelectric current as functions of the vertical position of the laser beam. The results shown with circles, diamonds, and squares correspond to the laser source positions shown using the same markers in Figure 7.

QTF that is closest to the laser source position,  $(x, z)$ . Since this heating expands the inner surface of the tine near  $p$ —but not the outer surface—the QTF bends at  $p$ . Consequently, as the distance from  $p$  to the tip of the tine increases, the displacement of the tip, and hence the piezoelectric signal, also increases. We also observe that the amount of bending at  $p$  increases when the applied heat or mechanical stress increases. The results of numerical simulations (*not shown*) demonstrate that at  $p(x, z)$  the temperature is approximately constant and the stress has a smaller linear increase as the laser source position  $z$  decreases from 0.8 mm to 0 mm in the  $z$  direction. These observations explain the slight increase of the signal in this region. As  $z$  decreases below 0 mm, the temperature near the junction of the tuning fork increases. Since the stress is also largest near the tuning fork junction, the signal increases dramatically as  $z$  decreases from 0 mm to  $-0.137$  mm. In Figure 8(right), we plot the phase lag of the piezoelectric signal as a function of the laser beam position. Although thermal waves do not possess wave fronts, we can still interpret the ratio  $\phi/\omega$ , where  $\phi$  is the phase of  $T$  at a point  $p$ , as a time lag, i.e., as the difference in time between the source peak and the peak of the temperature  $T$  at  $p$  [32]. When  $0 < z < 0.8$ , the time lag is

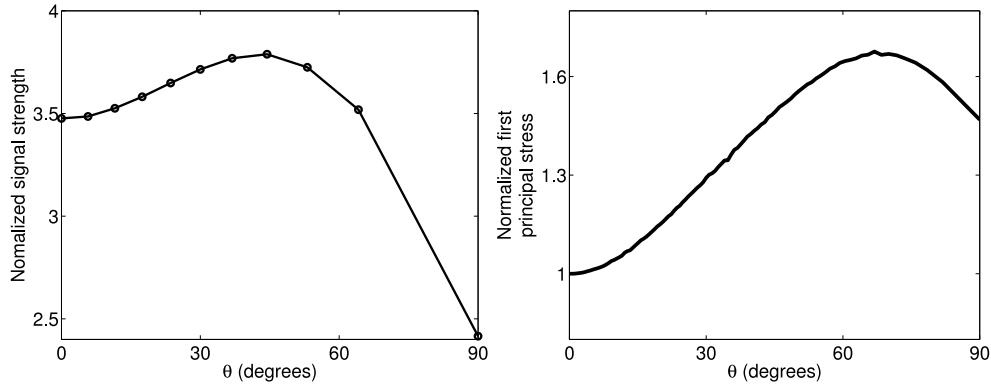


FIG. 9. Left: The amplitude of the piezoelectric current as a function of the angle from the negative vertical axis of the QTF. The laser source positions were chosen to lie on a circle of radius 0.0137 mm centered at the origin. Right: The first principal stress of the QTF as a function of the angle around a circle located between the tines of the QTF and at a distance of 0.02 mm from the inner surface.

approximately constant since the distance between the thermal source and the QTF is constant. When  $z < 0$ , the time lag is a linear function of the vertical distance from the source to the junction of the tines of the QTF. A physical interpretation of the slope of this linear function is given in the paper by Doty, Kosterev, and Tittel [12] for the laser positions shown with circles in Figure 8.

To more precisely determine the optimal position of the laser source, we performed an additional simulation in which we varied the source position around a quarter circle centered at the origin with a radius of 0.137 mm. All points on this circle were 0.013 mm from the inner surface of the QTF. In Figure 9(left), we plot the piezoelectric signal as a function of the angle,  $\theta$ , from the negative vertical axis of the QTF. The maximum of the signal occurs at  $\theta = 45^\circ$  and is 9% larger than the value at  $\theta = 0^\circ$ . However, in practice, it may be more prudent to position the laser at  $\theta = 0^\circ$  since the signal decreases rapidly as  $\theta$  increases above  $45^\circ$ . In Figure 9(right), we plot the first principal stress of the QTF as a function of the angle,  $\theta$ , around the circle centered at the origin and located in the QTF at a distance of 0.02 mm from the inner surface. For these results the stress was computed at the resonance frequency. The results in Figure 9 show that the maximum of the piezoelectric current at  $\theta = 45^\circ$  occurs near the maximum of the stress at  $\theta = 65^\circ$ . The discussion in this section suggests that the QTF that optimizes the piezoelectric signal will have long tines to allow for large bending and large stress near the junction of the tines to efficiently convert the thermal wave to a mechanical vibration.

To study the dependence of the slope of the signal amplitude on ambient pressure, in Figure 10(left) we plot the amplitude of the ROTADE signal as a function of the vertical position of the laser source for CO<sub>2</sub> at ambient pressures of 5, 10, and 20 Torr. On the right in Figure 10, we show a semilog plot of the same results. The figure indicates that the magnitude of the slope of the amplitude decreases as we decrease the ambient pressure. This behavior is primarily due to the fact that the thermal diffusivity,  $\kappa$ , of the gas is inversely proportional to the ambient pressure,  $P$  (on the other hand, it depends only weakly on the pressure dependence of the  $Q$ -factor).

**6.2. Comparison with results from laboratory experiments.** In this section we validate the model by comparing results obtained from numerical simulation

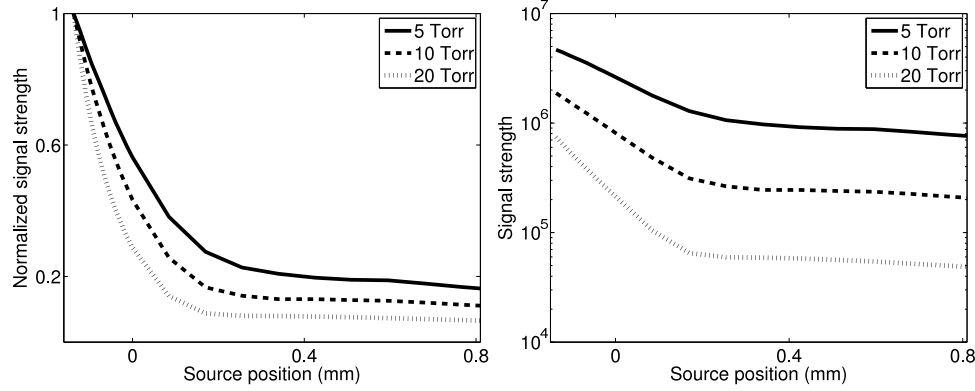


FIG. 10. The normalized amplitude of the ROTADE signal obtained from numerical simulations as a function of laser positions on a linear scale (left) and a log scale (right). These results are for CO<sub>2</sub> at three ambient pressures: 5, 10, and 20 Torr shown with solid, dashed, and dotted lines, respectively. The magnitude of the slope of the amplitude decreases as we decrease the ambient pressure.

and laboratory experiments. These results were obtained for 0.5% acetylene in nitrogen (C<sub>2</sub>H<sub>2</sub>:N<sub>2</sub>) and for pure carbon dioxide (CO<sub>2</sub>) at an ambient pressure of 20 Torr.

In Figure 11(left), we plot the amplitude of the ROTADE signal as a function of the vertical position,  $z$ , of the laser source for acetylene at 20 Torr. The amplitude curve from the simulations (solid line) was normalized to agree with the data from the experiments (circles) near  $z = 0$ . Both results show that the ROTADE signal is largest when the laser source is positioned near the base of the QTF. The slopes of the two amplitude curves agree for  $z < 0.25$  mm. In Figure 11(right), we plot the phase of the signal obtained from simulations (solid line) and experiments (circles). The experimental curve was shifted to account for a constant phase offset due to the electronics. We attribute the lack of agreement between the simulation results and the experimental data when  $z > 0.25$  mm in Figure 11 to the influence of the QEPAS signal, which we did not include in the simulation model. In the experimental data, the behavior near  $z = 0.5$  mm is due to destructive interference between the QEPAS and ROTADE signals. As  $z$  increases above 0.5 mm the QEPAS signal dominates, whereas for  $z < 0.25$  mm the ROTADE signal is dominant.

Next, we repeated the simulations for pure CO<sub>2</sub> at an ambient pressure of 20 Torr. In Figure 12(left), we plot the normalized amplitude of the signal obtained from simulations (solid line) and laboratory experiments (circles), and in Figure 12(right) we plot the phase of the signal. Near the junction of the tines the decay rate of the amplitude from the numerical simulation is about twice as large as the decay rate of the amplitude from experiment. The corresponding phase, however, is in better agreement than that seen for the amplitude. In Table 4, we give the slopes of the log of the amplitude (left) and of the phase (right) for C<sub>2</sub>H<sub>2</sub>:N<sub>2</sub> and for CO<sub>2</sub> at 20 Torr computed near the base of the QTF from the numerical simulation and experiment (see Figures 11 and 12). These results indicate that for CO<sub>2</sub> the decay rate of the modeled amplitude is almost twice as large as the decay rate of the experimentally observed amplitude. The phase slopes are in better agreement. On the other hand, for C<sub>2</sub>H<sub>2</sub>:N<sub>2</sub>, the slopes agree well for both the amplitude and the phase.

We attribute the discrepancy between the slopes obtained from the simulation and experiment in Figure 12 to the molecular dynamics of pure CO<sub>2</sub> which we did

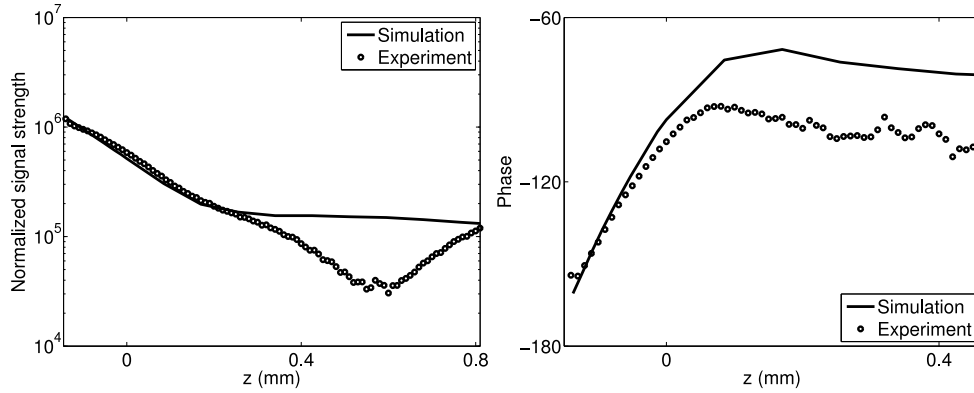


FIG. 11. Left: Amplitude of the ROTADE signal as a function of laser source position. Right: Phase of the ROTADE signal. The solid lines correspond to numerical simulation results and the circles correspond to laboratory experiments. The results in both plots correspond to experiments done using  $C_2H_2:N_2$  at an ambient pressure of 20 Torr.

not model. Specifically, when the laser interacts with  $CO_2$ , four vibrational quanta are added to each ground state  $CO_2$  molecule that is excited. However, only a small fraction of the  $CO_2$  molecules are excited. When excited molecules collide with the solid surface of the QTF, the most probable process is the transfer of one quantum of vibrational energy to the surface. It is known that different molecules have different probabilities of vibrational deactivation when colliding with a solid surface [55]. When an excited molecule collides with the solid surface of the QTF, the intramolecular potential is perturbed, and according to quantum perturbation theory, single-quantum transitions have the highest probability [35]. That is, the most probable process is the transfer of one quantum of vibrational energy to the surface. Therefore we may assume that the amount of heat transferred to the surface is proportional to the number of excited molecules that collide with it, regardless of the excitation level (number of vibrational quanta) of each excited molecule. When a highly excited  $CO_2$  molecule collides with a molecule in the ground state, there is a high probability of a resonant transfer of one vibrational quantum to the nonexcited molecule. Consequently, the number of excited molecules increases as the gas diffuses. Therefore, for pure  $CO_2$ , the process by which energy is transferred from the laser to the QTF is not accurately modeled by the classical heat equation. In fact, the increased concentration of excited molecules results in a slower decay of the thermal wave than is predicted by the heat equation. To accurately model the energy transfer process would require a coupled system of diffusion and kinetic rate equations that model the interactions among the various quantum states of  $CO_2$  molecules. As the parameters in the kinetic rate equations are difficult to determine we were not able to include this effect in our model. The reason we obtained such good agreement for the case of 0.5% acetylene in nitrogen is that, as is typical for trace gases, collisions between acetylene molecules occur with negligible probability due to the small concentration of acetylene.

**6.3. Numerical optimization.** We begin this section by presenting the computational details of applying the MADS algorithm to the frequency-constrained and frequency-unconstrained optimization problems. We used the 32.8 kHz QTF as a starting point for the optimization. We refer to this QTF as the *standard* 32.8 kHz QTF. We set the initial mesh size  $\Delta_0 = 10^{-5}$ , and for the search strategy we set the

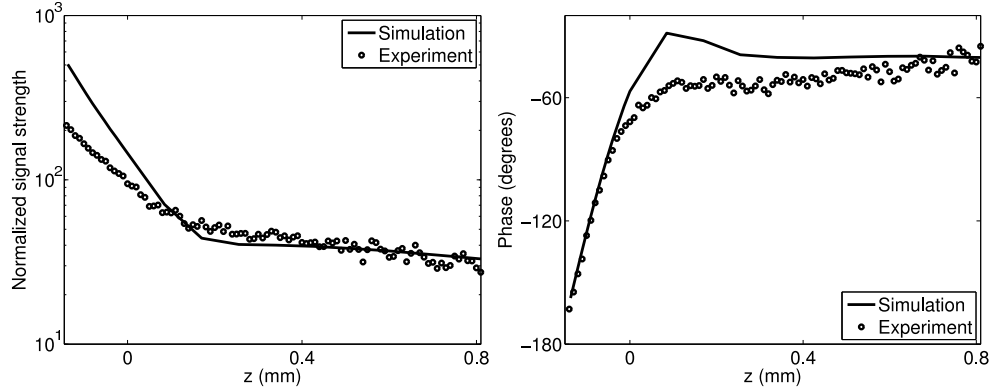


FIG. 12. Left: Amplitude of the ROTADE signal as a function of laser source position. Right: Phase of the ROTADE signal. The solid lines correspond to numerical simulation results and the circles correspond to laboratory experiments. The results in both plots correspond to experiments done using CO<sub>2</sub> at an ambient pressure of 20 Torr.

TABLE 4  
The slopes of the log of the amplitude and of the phase for the ROTADE signal.

(a) Amplitude			(b) Phase		
Gas	Simulation	Experiment	Gas	Simulation	Experiment
C <sub>2</sub> H <sub>2</sub> :N <sub>2</sub>	2.53	2.15	C <sub>2</sub> H <sub>2</sub> :N <sub>2</sub>	352	307
CO <sub>2</sub>	3.84	2.33	CO <sub>2</sub>	691	765

number of trial points to 100 for the frequency-constrained problem and to 200 for the frequency-unconstrained problem. The elements of the direction set  $D$  are the Euclidean coordinate directions and their negatives. We accept a point as optimal when the mesh size falls below  $10^{-6}$ . In these simulations the  $Q$ -factor was fixed at 39897, and the gas under study was CO<sub>2</sub> (the corresponding parameters are given in section 5.3). The bounds for the geometric parameters which describe the QTF were chosen based on existing off-the-shelf tuning forks and are listed in Table 5. In the previous section we described the difficulty we had in matching the numerical simulation results for pure CO<sub>2</sub> with experimental data. However, we do not expect that the tuning fork optimization results will markedly depend on the particular gas.

The optimal solutions are presented in Table 6. In the second column we list the parameters of the standard 32.8 kHz QTF. In columns 3 and 4 we give the optimal solution of the frequency-constrained and frequency-unconstrained problems, respectively. These results show that the signal strength of ROTADE sensors with a 30 kHz QTF can be improved by almost three times by optimizing the geometry of the QTF. If the resonance frequency is not constrained to lie near 30 kHz, the signal increases about 24 times. If we compare columns 2 and 3, we note that although the length of the tines did not change much, all the other parameters decreased from 25% to 50%. If the QTF is thinner and the length of the tines is large relative to the base, then under approximately the same applied stress one would expect a larger vibration. Column 4 shows that a 3 kHz QTF leads to a much larger signal. We note that the length and thickness of the tines of this tuning fork are about twice the length and

TABLE 5

The lower and upper bounds for the parameters of the tuning fork for the optimization study: length ( $l$ ), width ( $w$ ), gap ( $g$ ), length of the base ( $l_b$ ), and thickness ( $t$ ).

Parameter	Lower bound	Upper bound	SI unit
$l$	2	8	mm
$w$	0.2	0.8	mm
$g$	0.18	0.6	mm
$l_b$	1	4	mm
$t$	0.2	0.6	mm

TABLE 6

Numerical results from solving the design problems in which we optimize the geometry of the tuning fork. Problem parameters include  $f$  (numerical resonance frequency), length ( $l$ ), width ( $w$ ), gap ( $g$ ), length of the base ( $l_b$ ), and thickness ( $t$ ). The optimal values of the objective function,  $v_L$  (the velocity of the tines of the QTF), are shown in the last row.

Parameter	Standard 32.8 kHz QTF	Frequency-constrained optimum QTF	Frequency-unconstrained optimum QTF	SI unit
$f$	33.77	30.04	3.03	kHz
$l$	3.75	3.11	7.99	mm
$w$	0.6	0.34	0.20	mm
$g$	0.3	0.20	0.19	mm
$l_b$	2.33	1.76	2.04	mm
$t$	0.34	0.21	0.59	mm
$v_L$	0.06	0.18	1.47	m/s

thickness of the tines of the 30 kHz QTF, but the width of the tines is smaller. The iteration history for the frequency-constrained problem is shown in Figure 13.

In Figures 14, 15, and 16 we plot the first principal stress at the resonance frequency for the 32.8 kHz, 30 kHz, and 3 kHz QTFs, respectively. In all three cases the stress is largest near the junction of the tines of the QTFs. The maximum stress of the 32.8 kHz QTF is larger than the maximum stress of both the 30 kHz and 3 kHz QTFs. Therefore, we primarily attribute the increases in performance to the longer lengths and smaller widths of the optimal QTFs.

**7. Conclusions.** We have developed the first mathematical model for ROTADE sensors. With ROTADE sensing, a trace gas converts optical radiation to heat which is detected due to the induced thermoelastic deformation of a QTF. We studied the effect of the thermal source position on the ROTADE signal and validated experimental results which show that the signal is largest when the source is focused near the junction of the tines.

To validate the model, we used numerical simulations and experiments for 0.5% acetylene in nitrogen ( $C_2H_2:N_2$ ) and for pure carbon dioxide ( $CO_2$ ) to determine the amplitude and phase of the piezoelectric current as functions of the position of the laser beam. The simulation results agree with the experimental data for acetylene. For pure  $CO_2$ , the experimental decay of the diffusion wave is slower than that predicted by the numerical simulations since the model does not accurately capture the molecular

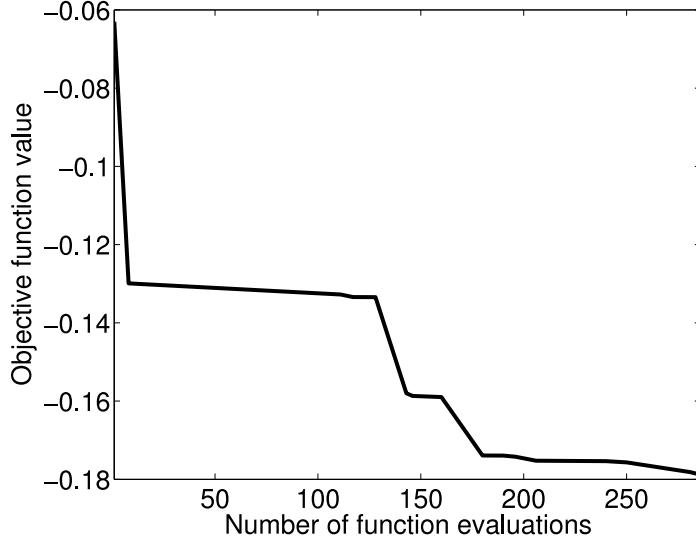


FIG. 13. Progression of the objective function value versus the number of evaluations for the frequency-constrained optimization problem.

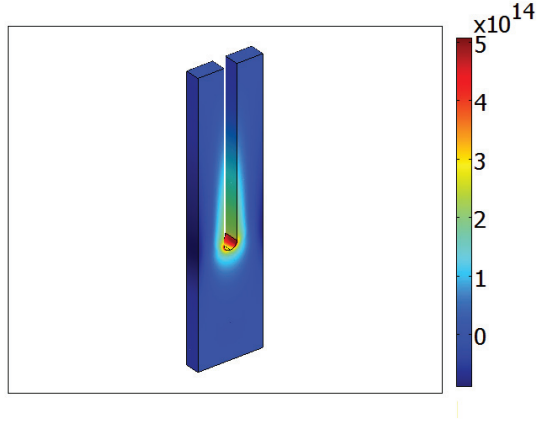


FIG. 14. The first principal stress (Pa) of the 32.8 kHz QTF at the resonance frequency.

dynamics of pure CO<sub>2</sub>. The reason we obtained such good agreement in the case of C<sub>2</sub>H<sub>2</sub>:N<sub>2</sub> is that there was a much smaller probability of C<sub>2</sub>H<sub>2</sub> to C<sub>2</sub>H<sub>2</sub> collisions since the concentration of acetylene was only 0.5%. For actual trace gas sensing applications, we expect the classical heat equation model to be good enough since the trace gas to be detected would typically have a very low concentration in the ambient air.

We also optimized the geometry of the QTF for a ROTADE sensor. We used the MADS algorithm to solve the optimization problem with and without frequency constraints. Our simulations show that the optimally shaped QTF (with the resonance frequency constrained close to 32.8 kHz) produces a ROTADE signal that is three

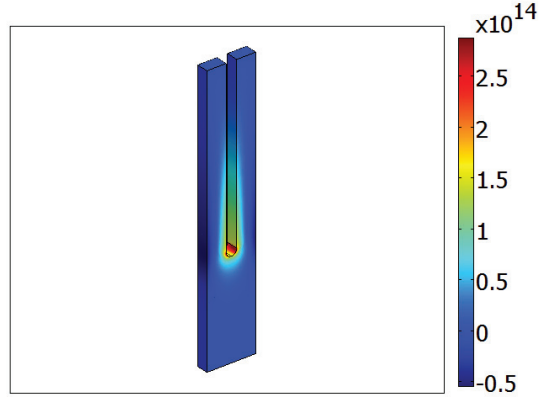


FIG. 15. *The first principal stress (Pa) of the 30 kHz QTF at the resonance frequency.*

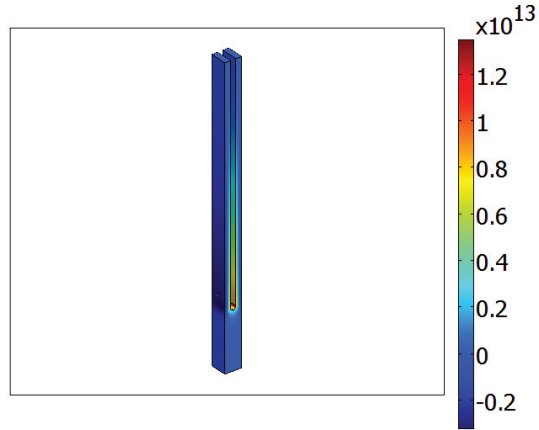


FIG. 16. *The first principal stress (Pa) of the 3 kHz QTF at the resonance frequency.*

times larger than the signal obtained with the standard 32.8 kHz tuning fork. We also ran a simulation in which the resonance frequency was unconstrained and found that by using a 3 kHz QTF the ROTADE signal can be increased by a factor of about 24 relative to the standard QTF. We attribute the large increase in the piezoelectric signal to the large changes in the width and the length of the tines of the QTF.

Future ROTADE modeling research may focus on the molecular interaction of trace gases. One could replace the heat equation by a coupled system of partial differential equations that models the diffusion of and interaction among molecules in several different energy states. To date we have fixed the quality factor which plays a role in the damping of the tuning fork vibration. Since this parameter will change with the QTF geometry, in future work we plan to develop a method to automatically compute the quality factor in terms of the QTF geometry.

**Acknowledgments.** We thank Mike Stone (Sandia National Labs), Manil Suri, Mike Reid, Florian Potra (UMBC), Frank Tittel, and Steve Cox (Rice University) for helpful discussions.

## REFERENCES

- [1] M. A. ABRAMSON, *Pattern Search Algorithms for Mixed Variable General Constrained Optimization Problems*, Ph.D. thesis, Department of Computational and Applied Mathematics, Rice University, Houston, TX, 2002.
- [2] M. A. ABRAMSON, *NOMADm version 4.6 User's Guide*, Department of Mathematics and Statistics, Air Force Institute of Technology, WPAFB, OH, 2007.
- [3] M. A. ABRAMSON, C. AUDET, AND J. E. DENNIS, JR., *Nonlinear programming with mesh adaptive direct searches*, SIAG/Optimization Views-and-News, 17 (2006), pp. 2–11.
- [4] S. N. AHMAD, C. S. UPADHYAY, AND C. VENKATESAN, *Electro-thermo-elastic formulation for the analysis of smart structures*, Smart Mater. Struct., 15 (2006), pp. 401–416.
- [5] C. ASHCRAFT AND R. GRIMES, *SPOOLES: An object-oriented sparse matrix library*, in Proceedings of the Ninth SIAM Conference on Parallel Processing for Scientific Computing, 1999.
- [6] C. AUDET AND J. E. DENNIS, JR., *A pattern search filter method for nonlinear programming without derivatives*, SIAM J. Optim., 14 (2004), pp. 980–1010.
- [7] C. AUDET AND J. E. DENNIS, JR., *Mesh adaptive direct search algorithms for constrained optimization*, SIAM J. Optim., 17 (2006), pp. 188–217.
- [8] A. G. BELL, *On the production and reproduction of sound by light*, Am. J. Sci., 20 (1880), pp. 305–324.
- [9] A. G. BELL, *Upon the production of sound by radiant energy*, Phil. Mag. J. Sci., 21 (1881), pp. 510–528.
- [10] D. E. CARLSON, *Linear thermoelasticity*, in Mechanics of Solids II, C. Truesdell, ed., Springer-Verlag, Berlin, 1984, pp. 297–345.
- [11] COMSOL, *Multiphysics Modeling and Engineering Simulation Software*, <http://www.comsol.com>.
- [12] J. H. DOTY III, A. A. KOSTEREV, AND F. K. TITTEL, *First experimental studies of the resonant optothermoacoustic detection technique*, in Proceedings of the Conference on Lasers and Electro-Optics, Optical Society of America, Washington, DC, 2010, paper CPDB12.
- [13] S. L. FIREBAUGH, F. ROIGNANT, AND E. A. TERRAY, *Modeling the response of photoacoustic gas sensors*, in Proceedings of the COMSOL Conference, 2009.
- [14] S. L. FIREBAUGH, F. ROIGNANT, AND E. A. TERRAY, *Enhancing sensitivity in tuning fork photoacoustic spectroscopy systems*, in Proceedings of the IEEE Sensors Applications Symposium, 2010, pp. 30–35.
- [15] A. P. FRENCH, *Vibrations and Waves*, Norton & Company, New York, 1971.
- [16] G. GAUTSCHI, *Piezoelectric Sensorics*, Springer, Heidelberg, 2002.
- [17] G. H GOLUB AND C. F VAN LOAN, *Matrix Computations*, The Johns Hopkins University Press, Baltimore, MD, 1989.
- [18] R. D. GROBER, J. ACIMOVIC, J. SCHUCK, D. HESSMAN, P. J. KINDLEMAN, J. HESPAHNA, A. S. MORSE, K. KARRAÏ, I. TIEMANN, AND S. MANUS, *Fundamental limits to force detection using quartz tuning forks*, Rev. Sci. Instrum., 71 (2000), pp. 2776–2780.
- [19] M. HIRATA, K. KOKUBUN, M. ONO, AND K. NAKAYAMA, *Size effect of a quartz oscillator on its characteristics as a friction vacuum gauge*, J. Vac. Sci. Technology A, 3 (1985), pp. 1742–1745.
- [20] S. S. HOWARD, Z. J. LIU, D. WASSERMAN, A. HOFFMAN, T. KO, AND C. F. GMACHL, *High-performance quantum cascade lasers: Optimized design through waveguide and thermal modeling*, IEEE J. Select. Topics Quantum Electron., 13 (2007), pp. 1054–1064.
- [21] H. ITOH, Y. AOSHIMA, AND Y. SAKAGUCHI, *Model for a quartz-crystal tuning fork using plate spring approximated to torsion spring adopted at the joint of the arm and the base*, in Proceedings of the IEEE International Frequency Control Symposium and PDA Exhibition, 2002, pp. 145–151.
- [22] K. KARRAÏ AND R. D. GROBER, *Piezo-electric tuning fork tip-sample distance control for near field optical microscopes*, Ultramicroscopy, 61 (1995), pp. 197–205.
- [23] A. A. KOSTEREV AND S. M. BACHILLO, *Resonant Optothermoacoustic Detection of Optical Absorption*, United States Patent Application 20090174884.
- [24] A. A. KOSTEREV, Y. A. BAKHIRKIN, R. F. CURL, AND F. K. TITTEL, *Quartz-enhanced photoacoustic spectroscopy*, Optics Letters, 27 (2002), pp. 1902–1904.

- [25] A. A. KOSTEREV AND J. H. DOTY III, *Resonant optothermoacoustic detection: Technique for measuring weak optical absorption by gases and micro-objects*, Optics Letters, 35 (2010), pp. 3571–3573.
- [26] A. A. KOSTEREV, F. K. TITTEL, D. V. SEREBRYAKOV, A. L. MALINOVSKY, AND I. V. MOROZOV, *Applications of quartz tuning forks in spectroscopic gas sensing*, Rev. Sci. Instrum., 76 (2005), pp. 431051–431059.
- [27] A. A. KOSTEREV, G. WYSOCKI, Y. BAKHIRKIN, S. SO, R. LEWICKI, M. FRASER, F. K. TITTEL, AND R. F. CURL, *Application of quantum cascade lasers to trace gas analysis*, Appl. Phys. B, 90 (2007), pp. 165–176.
- [28] S. LEE, *Design optimization of surface mount device 32.768 kHz quartz tuning fork-type crystals using finite element method and statistical analysis of test samples manufactured using photolithography*, Vacuum, 68 (2003), pp. 139–148.
- [29] R. M. LEWIS AND V. TORCZON, *Pattern search algorithms for bound constrained minimization*, SIAM J. Optim., 9 (1999), pp. 1082–1099.
- [30] A. MANDELIS, *Photoacoustic and Thermal Wave Phenomena in Semiconductors*, Elsevier, New York, 1996.
- [31] A. MANDELIS, *Diffusion waves and their use*, Phys. Today, 53 (2000), pp. 29–34.
- [32] A. MANDELIS, *Diffusion-Wave Fields: Mathematical Methods and Green Functions*, Springer, Berlin, 2001.
- [33] W. A. MARRISON, *The evolution of the quartz crystal clock*, Bell System Tech. J., 27 (1948), pp. 510–588.
- [34] M. R. MCCURDY, Y. BAKHIRKIN, G. WYSOCKI, R. LEWICKI, AND F. K. TITTEL, *Recent advances of laser-spectroscopy based techniques for applications in breath analysis*, J. Breath Res., 1 (2007), pp. 14001–140013.
- [35] A. MESSIAH, *Quantum Mechanics*, Vol. II, North-Holland, Amsterdam, 1965.
- [36] A. MIKLOS, Z. BOZOKI, Y. JIANG, AND M. FEHER, *Experimental and theoretical investigation of photoacoustic-signal generation by wavelength-modulated diode lasers*, Appl. Phys. B, 58 (1994), pp. 483–492.
- [37] A. MIKLOS, P. HESS, AND Z. BOZOKI, *Application of acoustic resonators in photoacoustic trace gas analysis and metrology*, Rev. Sci. Instrum., 72 (2001), pp. 1937–1955.
- [38] NIST, *Chemistry WebBook*, NIST Standard Reference Database Number 69, available online from <http://webbook.nist.gov/chemistry/>.
- [39] J. F. NYE, *Physical Properties of Crystals*, Oxford University Press, New York, 2000.
- [40] J. A. PELESKO, *Nonlinear stability considerations in thermoelastic contact*, Trans. ASME J. Appl. Mech., 66 (1999), pp. 109–116.
- [41] J. A. PELESKO, *Nonlinear stability, thermoelastic contact and the Barber condition*, Trans. ASME J. Appl. Mech., 68 (2001), pp. 28–33.
- [42] N. PETRA AND M. K. GOBBERT, *Parallel performance studies for COMSOL Multiphysics using scripting and batch processing*, in Proceedings of the COMSOL Conference, 2009.
- [43] N. PETRA, A. A. KOSTEREV, J. ZWECK, S. E. MINKOFF, AND J. H. DOTY III, *Numerical and experimental investigation for a resonant optothermoacoustic sensor*, in Proceedings of the Conference on Lasers and Electro-Optics, Optical Society of America, Washington, DC, 2010, paper CMJ6.
- [44] N. PETRA, J. ZWECK, A. A. KOSTEREV, S. E. MINKOFF, AND D. THOMAZY, *Theoretical analysis of a quartz-enhanced photoacoustic spectroscopy sensor*, Appl. Phys. B, 94 (2009), pp. 673–680.
- [45] D. D. QUINN AND J. A. PELESKO, *Generic unfolding of the thermoelastic contact instability*, Internat. J. Solids Structures, 39 (2002), pp. 145–157.
- [46] T. H. RISBY AND S. F. SOLGA, *Current status of clinical breath analysis*, Appl. Phys. B, 85 (2006), pp. 421–426.
- [47] A. ROSENZWAIG, *Photoacoustics and Photoacoustic Spectroscopy*, Wiley, New York, 1980.
- [48] L. S. ROTHMAN, I. E. GORDON, A. BARBE, D. CHRIS BENNER, P. F. BERNATH, M. BIRK, V. BOUDON, L. R. BROWN, A. CAMPARGUE, J. P. CHAMPION, K. CHANCE, L. H. COUDERT, V. DANA, V. M. DEVI, S. FALLY, J. M. FLAUD, R. R. GAMACHE, A. GOLDMAN, D. JACQUEMART, I. KLEINER, N. LACOME, W. J. LAFFERTY, J. Y. MANDIN, S. T. MASSIE, S. N. MIKHAILENKO, C. E. MILLER, N. MOAZZEN-AHMADI, O. V. NAUMENKO, A. V. NIKITIN, J. ORPHAL, V. I. PEREVALOV, A. PERRIN, A. PREDOI-CROSS, C. P. RINSLAND, M. ROTGER, M. SIMECKOVA, M. A. H. SMITH, K. SUNG, S. A. TASHKUN, J. TENNYSON, R. A. TOTH, A. C. VANDAELE, AND J. VAN DER AUWERA, *The HITRAN 2008 molecular spectroscopic database*, J. Quant. Spectrosc. Radiat. Transf., 110 (2009), pp. 533–572.
- [49] D. V. SEREBRYAKOV, A. P. CHERKUN, B. A. LOGINOV, AND V. S. LETOKHOV, *Tuning-fork-based fast highly sensitive surface-contact sensor for atomic force microscopy/near-field*

- scanning optical microscopy, Rev. Sci. Instrum., 73 (2002), pp. 1795–1802.
- [50] A. E. SIEGMAN, *Lasers*, University Science Books, Mill Valley, CA, 1986.
  - [51] M. STEIN, Large sample properties of simulations using Latin hypercube sampling, Technometrics, 29 (1987), pp. 143–151.
  - [52] D. B. SULLIVAN, Time and frequency measurement at NIST: The first 100 years, in Proceedings of the IEEE International Frequency Control Symposium and PDA Exhibition, 2001, pp. 4–17.
  - [53] V. TORCZON, On the convergence of pattern search algorithms, SIAM J. Optim., 7 (1997), pp. 1–25.
  - [54] L. N. TREFETHEN AND D. BAU III, *Numerical Linear Algebra*, SIAM, Philadelphia, 1997.
  - [55] L. S. VASILENKO, A. A. KOVALEV, AND N. N. RUBTSOVA, Laser optothermal spectroscopy in gases, Laser Phys., 2 (1992), pp. 883–891.
  - [56] M. D. WOJCIK, M. C. PHILLIPS, B. D. CANNON, AND M. S. TAUBMAN, Gas-phase photoacoustic sensor at  $8.41\text{ }\mu\text{m}$  using quartz tuning forks and amplitude-modulated quantum cascade lasers, Appl. Phys. B, 11 (2006), pp. 307–313.
  - [57] Y. ZHANG, J. A. SMITH, A. P. MICHEL, M. L. BAECK, Z. WANG, J. D. FAST, AND C. GMACHL, Coupled Monitoring and Modeling of Air Quality and Regional Climate during the 2008 Beijing Olympic Games, abstract A14A-03, American Geophysical Union, Fall Meeting 2009, San Francisco, 2009.